

Highly sensitive NH₃ gas sensor based on the porous Ce_{0.94}Zr_{0.06}O₂ nano-sheets with ppb level detection limit

Zhijie Li¹, Junqiang Wang¹, Sa Zhang¹, Shengnan Yan¹, Baobao Cao², Wenzhong Shen³, Zhiguo Wang^{1*}, Yong Qing Fu^{4*}

¹School of Physical Electronics, University of Electronic Science and Technology of China, Chengdu 610054, PR China

²A Key Laboratory of Advanced Technologies of Materials, Ministry of Education, Southwest Jiaotong University, Chengdu 610031, China

³State Key Laboratory of Coal Conversion, Institute of Coal Chemistry, Chinese Academy of Sciences, Taiyuan 030001, PR China

⁴Faculty of Engineering and Environment, Northumbria University, Newcastle Upon Tyne, NE1 8ST, United Kingdom

Abstract

Porous Ce_{0.94}Zr_{0.06}O₂ nano-sheets sensing material was synthesized using a facile sol-hydrothermal process. The average thickness of the Ce_{0.94}Zr_{0.06}O₂ nano-sheets was about 8 nm, and the nano-sheets were found to have a mesoporous structure with an average pore size around 2.1 nm. The mesoporous structure of Ce_{0.94}Zr_{0.06}O₂ nano-sheets resulted in larger specific surface areas of 185.4 m²/g and more pore volumes of 0.51 cm³/g than those of CeO₂, which was beneficial to the absorption of target gas. Due to the special mesoporous structures in the nano-sheets and the plenty of hydroxyl groups on the surface, the NH₃ sensors made of the porous Ce_{0.94}Zr_{0.06}O₂ nano-sheets showed a higher sensitivity (87 to 100 ppm NH₃) and a lower detection limit (100 ppb) at room temperature than the sensors made of pure CeO₂ nano-sheets prepared using the similar process. And they exhibited good selectivity, reproducibility and long-term stability to NH₃ detection at room temperature.

Keywords: CeO₂, Nano-sheets; Porous; Sol-hydrothermal; Gas sensor

1. Introduction

CeO₂ based nanomaterials have attracted considerable attention in recent years due to their optical and magnetic properties, superior catalytic performance, oxygen storage capacity and excellent gas sensing performance. They have found a wide range of applications in catalysis [1, 2], storage oxygen materials [3], fuels cells [4], supercapacitors [5], ferromagnetic oxides [6], gas sensors [7-10] and luminescence materials [11, 12]. Various CeO₂ based nanostructures have been synthesized using sol-gel method [13], electro-spinning [14, 15], hydrothermal method [16-20], and precipitation method [21, 22]. These nanostructural morphologies generally include nanoparticles [13, 22], nanowires [18], nanorods [17, 19], nanosheets [16, 17], nanofiber [14, 15] and nanoflowers[20], which can be successfully used as gas sensing materials. For example, Liao *et al.* [23] made a gas sensor using CeO₂ nanowires decorated with Pt nanocrystals prepared using a hydrothermal method, and the sensor showed a good selectivity for detection of CO. Barreca *et al.* [24] synthesized CeO₂ columnar nanostructures using a chemical vapour deposition method and demonstrated their high sensitivity for detection of gaseous ethanol and nitrogen dioxide. Lei *et al.* [9] prepared CeO₂ nanofibers using a two-step electrospinning and calcination method for real-time CO sensing. Michela *et al.* [25] prepared hollow CeO₂ microspheres with 3D architectures using a microwave-assisted coprecipitation method for detection of CO. Yang *et al.* [26] synthesized CeO₂/graphene-like nano-sheet composites using a solvothermal method

for sensing NO_x gas.

Among these CeO₂ nanostructures, porous nano-sheets would be one of the best nanostructures for gas sensing due to their extremely high surface-to-volume ratio and thus effective adsorption of gas molecules. Doping various elements into CeO₂ is commonly regarded as a good method to further improve its sensing properties and these elements include Ti [27], B [28], Zn [29] and In [15]. Zr-doped CeO₂ was previously applied to enhance catalytic property [30, 31]. The improved catalytic performance would be beneficial for its gas sensing performance. The addition of Zr can significantly and effectively prevent the rapid growth of CeO₂ crystallite size, thus maintaining a small crystal sizes in the nanostructures. This can provide a larger specific surface area and higher pore volumes than those of CeO₂ nanostructures, thus would be beneficial for improvement in gas sensing performance. However, up to now, preparation of porous nano-sheets structures of Zr-doped CeO₂ and characterization of their gas sensing mechanisms have never been explored.

In the study, we prepared Zr doped CeO₂ porous nano-sheet structures using a facile surfactant-free sol-hydrothermal process. These Ce_{0.94}Zr_{0.06}O₂ nano-sheets showed excellent NH₃ sensing performance at room temperature than pure CeO₂ nano-sheets, which was prepared using the similar process. The Zr doped CeO₂ nanoporous structures have been characterized thoroughly in this paper, and their NH₃ sensing performance and mechanisms have been investigated.

2. Experimental procedures

2.1 Synthesis of samples

Zr doped CeO₂ samples were prepared using a sol-hydrothermal process. All chemicals used in the synthesis processes were of analytical grade purity. In order to prepare Ce_{0.94}Zr_{0.06}O₂ nano-sheets, 10 milli-mol (mmol) Ce(NO₃)₃·6H₂O, 1 mmol ZrO(NO₃)₂·2H₂O, and 5 mmol NaNO₃ were dissolved into 80 ml deionized water under a constant stirring to form a transparent solution. Ammonia (NH₃·H₂O, 27%) of 20 ml was added into the solution drop-by-drop within 10 min under a continuous stirring to form a yellow semi-transparent sol. Subsequently, 2 mL hydrogen peroxide (H₂O₂) was dropped into the sol. The sol was continually stirred for about 30 min until the color of the sol was turned into reddish-brown. Then the obtained reddish-brown sol was hydrothermally reacted at 100 °C Teflon-lined stainless steel autoclave of 120 mL for 20 hours. Finally, the hydrothermal precipitates were filtered by distilled water and dried at 60 °C for 10 hours to obtain light-yellow Ce_{0.94}Zr_{0.06}O₂ powder samples. Using the same process, the pure CeO₂ sample was prepared without addition of ZrO(NO₃)₂·2H₂O in the reaction.

2.2 Characterization

X-ray diffraction (XRD, CuK α , 40kV, 60mA, Rigaku D/max-2400) was conducted to characterize the crystalline structure and average crystalline sizes of samples. Morphologies and micro/nanostructures of samples were studied using Inspect F50 scanning electron microscope (SEM) and JEOL 2010 F field emission gun electron microscope (TEM). Energy-dispersive X-ray spectroscopy (EDX) analysis was carried out to obtain the dot-mapping of various elements in nano-sheets. Thickness of nano-sheet was measured using an atomic force microscope (AFM, CSPM4000). A

nitrogen physisorption apparatus of JW-BK122W was used to measure the nitrogen adsorption-desorption isotherms of samples at 77 K. Prior to N₂ physisorption, all the samples were dehydrated at 200 °C for 2 hours under a vacuum. The pore diameter distribution and specific surface area were obtained using density functional theory (DFT) and Brunauer–Emmett–Teller (BET) method, respectively. The total pore volumes (V_{total}) were calculated using the adsorption amount at P/P₀ of 0.99. X-ray photoelectron spectroscopy (XPS, Kratos Axis-Ultra DLD apparatus with Al K α radiation) was conducted to analyze the chemical states of different elements of samples. The element analysis of Zr was conducted by Inductive Coupled Plasma Emission Spectrometer (ICP, AtomScan 16, TJA, USA).

3. Results and discussion

3.1 Morphologies and structure of samples

XRD spectra of Ce_{0.94}Zr_{0.06}O₂ and pure CeO₂ samples are shown in **Fig. 1**. All the diffraction peaks of Ce_{0.94}Zr_{0.06}O₂ and CeO₂ are in a good agreement with JCPDS card for cubic fluorite CeO₂ (JCPDS NO. 34-0394). This indicates that for both CeO₂ and Ce_{0.94}Zr_{0.06}O₂, the fluorite cubic phase structure was synthesized by hydrothermal reaction without calcination. No peaks of any other phases could be detected, indicating that the Ce³⁺ was completely transformed into CeO₂ during the synthesis process. The crystallite sizes L of samples were estimated according to the Scherrer formula: $L = K\lambda/(\beta\cos\theta)$ ($\lambda=0.15406$ nm, $K=0.89$, β is the peak width at half height, and θ is the diffracting angle). The obtained crystallite sizes of CeO₂ and Ce_{0.94}Zr_{0.06}O₂ are 3.2 and 2.8 nm, respectively. The crystallite sizes of the

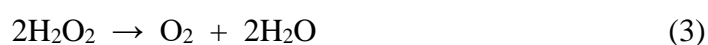
$\text{Ce}_{0.94}\text{Zr}_{0.06}\text{O}_2$ are smaller than that of CeO_2 , because the addition of Zr^{4+} could prevent the rapid growth of CeO_2 crystallite size. In addition, no characteristic peaks of the zirconium oxide in **Fig. 1** are observed in $\text{Ce}_{0.94}\text{Zr}_{0.06}\text{O}_2$. Due to similar ionic radii and Pauling electronegativity values of Zr^{4+} (0.072 nm) and Ce^{4+} (0.087 nm) ion, the Zr ions could substitute Ce^{4+} ones to form a stable substitutional solid solution. Moreover, the high-resolution of (111) peaks of XRD spectra of CeO_2 and $\text{Ce}_{0.94}\text{Zr}_{0.06}\text{O}_2$ samples were further compared (as shown in the Fig.S2). A small shift of the (111) peak to high angle is observed, which should result from the doping of Zr^{4+} in CeO_2 . It is also found that the characteristic peaks of $\text{Ce}_{0.94}\text{Zr}_{0.06}\text{O}_2$ have a weaker intensity and a larger half peak width than that of CeO_2 , indicating the decreasing of crystallinity and diameter of $\text{Ce}_{0.94}\text{Zr}_{0.06}\text{O}_2$ due to the Zr^{4+} doping in CeO_2 . Based on the above results, it can be confirmed that Zr^{4+} was successfully doped into the CeO_2 .

Fig. 2 shows the morphologies of pure CeO_2 and $\text{Ce}_{0.94}\text{Zr}_{0.06}\text{O}_2$ obtained from SEM and TEM analysis. Both CeO_2 and $\text{Ce}_{0.94}\text{Zr}_{0.06}\text{O}_2$ samples are consisted of a large number of nano-sheets from SEM images (**Figs. 2a** and **2d**) and TEM images (**Figs. 2b** and **2e**). Some wrinkle-like patterns could be observed in TEM image shown in **Figs. 2b** and **2e**, which is a common feature for the ultrathin nano-films [32]. AFM analysis (shown in **Fig. 3** and **Fig. S1**) reveal that thickness of $\text{Ce}_{0.94}\text{Zr}_{0.06}\text{O}_2$ nano-sheets is about 8 nm. Based on HRTEM images of $\text{Ce}_{0.94}\text{Zr}_{0.06}\text{O}_2$ nano-sheets shown in **Figs. 2c** and **2f**, both the CeO_2 and $\text{Ce}_{0.94}\text{Zr}_{0.06}\text{O}_2$ nano-sheets are composed of numerous nanoparticles. The diameters of CeO_2 and $\text{Ce}_{0.94}\text{Zr}_{0.06}\text{O}_2$ nano-particles

are in the range from 2 nm to 4 nm, which is in agreement with the results obtained from XRD analysis. The lattice spacing of 0.329 nm of pure CeO₂ (shown in **Fig. 2c**) agrees well with that of the (111) planes of the cubic CeO₂. The Ce_{0.94}Zr_{0.06}O₂ nano-crystal has a lattice spacing of 0.325 nm (see **Fig. 2f**), and the lattice spacing of the (111) planes is smaller than that of pure CeO₂ (0.329 nm) because of substitution of Ce⁴⁺ (0.087 nm) with Zr⁴⁺ (0.072 nm). The SAED patterns (see the inset images shown in **Figs. 2c** and **2f**) proves the good crystallization of CeO₂ and Ce_{0.94}Zr_{0.06}O₂, and they are correspondent to the fluorite phase structure of CeO₂.

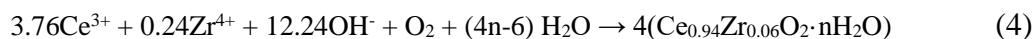
Figs. 4b and **4c** show the typical EDX elemental mapping of the Ce and Zr elements in Ce_{0.94}Zr_{0.06}O₂ sample (**Fig. 4a**). Clearly, Ce and Zr elements are homogeneously distributed in the Ce_{0.94}Zr_{0.06}O₂ nano-sheets as shown in **Figs. 4b** and **4c**, indicating the formation of a uniformly substitutional solid solution. This is consistent with the conclusion from the XRD analysis. Furthermore, the content of Zr in the CeO₂ is 6.0 % from the EDX analysis (see **Fig. S3** of the EDX pattern of Ce_{0.94}Zr_{0.06}O₂ nano-sheets). Moreover, the ICP analysis also found that the molar percentage of Zr in Ce_{0.94}Zr_{0.06}O₂ sample is 6.01%. Therefore, we define this nanomaterial as Ce_{0.94}Zr_{0.06}O₂.

In the synthesis process, ammonia (NH₃·H₂O) and H₂O₂ decompose and form OH⁻ and O₂ in aqueous solutions as listed in reaction formula (2) and (3):

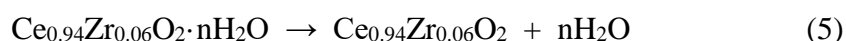


In the presence of O₂ in the alkaline solution, the Ce³⁺ ions are unstable and the

hydrated Ce^{4+} oxide can be easily formed. At the same time, the Zr^{4+} ions could enter into the lattice sites of CeO_2 by substituting Ce^{4+} ions to form $\text{Ce}_{0.94}\text{Zr}_{0.06}\text{O}_2 \cdot n\text{H}_2\text{O}$ according to the following reaction:



In the hydrothermal process, $\text{Ce}_{0.94}\text{Zr}_{0.06}\text{O}_2$ nanocrystals could be formed through crystallization of $\text{Ce}_{0.94}\text{Zr}_{0.06}\text{O}_2 \cdot n\text{H}_2\text{O}$ under elevated temperatures and pressure.



The porosity of the CeO_2 and $\text{Ce}_{0.94}\text{Zr}_{0.06}\text{O}_2$ nano-sheets were characterized and the N_2 adsorption-desorption isotherms and pore size distributions are shown in **Fig. 5**. Both the adsorption–desorption isotherms of CeO_2 and $\text{Ce}_{0.94}\text{Zr}_{0.06}\text{O}_2$ nano-sheets exhibit typical type-IV isotherms with a hysteresis loop that corresponds to a mesoporous structure. The pore size distribution of CeO_2 and $\text{Ce}_{0.94}\text{Zr}_{0.06}\text{O}_2$ nano-sheets are concentrated at around 2.5 nm and 2.1 nm, respectively, indicating the formation of mesoporous structures in the nano-sheets. The pores could be accumulated among the nanoparticles during their growth and coalescence. The mesoporous structures of nano-sheets result in large specific surface areas and pore volumes, which are beneficial to the absorption of target gas molecules during gas sensing. The specific surface area and pore volume of CeO_2 are $135.0 \text{ m}^2/\text{g}$ and $0.40 \text{ cm}^3/\text{g}$, respectively. Compared with the CeO_2 nano-sheets, the $\text{Ce}_{0.94}\text{Zr}_{0.06}\text{O}_2$ nano-sheets have a larger specific surface area and pore volume of $185.4 \text{ m}^2/\text{g}$ and $0.51 \text{ cm}^3/\text{g}$. Because of their smaller crystallite sizes, larger specific surface areas and pore volumes, the $\text{Ce}_{0.94}\text{Zr}_{0.06}\text{O}_2$ nano-sheets should have a better sensing

performance than pure CeO₂.

Fig. 6 shows the XPS results of the CeO₂ and Ce_{0.94}Zr_{0.06}O₂ nano-sheets. In **Fig. 6a**, both Ce 3d XPS spectra of CeO₂ and Ce_{0.94}Zr_{0.06}O₂ nano-sheets show six peaks at the binding energy of 881.9 eV, 887.9 eV, 897.9 eV, 900.4 eV, 906.9 eV and 916.1 eV, which are attributed to the characteristic of Ce (IV) 3d states with three pairs of spin-orbit splits [33]. The peaks located at 881.9 eV, 887.9 eV and 897.9 eV are corresponding to the Ce 3d_{5/2}, and the peaks at 900.4 eV, 906.9 eV and 916.1 eV are corresponding to the Ce 3d_{3/2}. The three pairs of binding energy (916.1 and 897.9 eV, 906.9 and 887.9 eV, 900.4 and 881.9 eV) are corresponding to the final state of Ce (IV) 3d⁹4f⁰ O2p⁶, Ce (IV) 3d⁹4f¹ O2p⁵ and Ce (IV) 3d⁹4f² O2p⁴, respectively [34]. This is in a good agreement with the characteristic chemical valence of Ce⁴⁺ ions. The results are consistent with the conclusions drawn from XRD analysis.

As illustrated in **Fig. 6b**, the O 1s XPS spectra of CeO₂ and Ce_{0.94}Zr_{0.06}O₂ nano-sheets show two obviously peaks at binding energies of 528.7 eV and 530.7 eV, respectively. The main peak centered at 528.7 eV is attributed to the lattice oxygen in the CeO₂ and Ce_{0.94}Zr_{0.06}O₂ crystals [34, 35]. The peak at a higher binding energy of 530.7 eV is indexed to hydroxyl group on the surface of nanoparticles [36]. It is obvious that there are much more hydroxyl groups on the surface of CeO₂ and Ce_{0.94}Zr_{0.06}O₂ nanoparticles due to the large peak areas at 530.7 eV.

The XPS spectrum of the Zr 3d of Ce_{0.94}Zr_{0.06}O₂ nano-sheets is shown in **Fig. 6c**. There are double peaks at binding energies of 182.0 and 184.4 eV, which are attributed to the Zr 3d_{5/2} and Zr 3d_{3/2} characteristic signals of chemical valence of

Zr⁴⁺ ions in the Ce_{0.94}Zr_{0.06}O₂ nano-sheets. The atomic ratio on the surface of sample could be estimated by the XPS peaks areas. The obtained Zr:Ce atomic ratios was 6.9:93.1 in the Ce_{0.94}Zr_{0.06}O₂ nano-sheets. The content of Zr on the surface of Ce_{0.94}Zr_{0.06}O₂ nano-sheets is close to the results of EDX.

3.2 Gas sensing properties of CeO₂ and Ce_{0.94}Zr_{0.06}O₂ nano-sheets based gas sensors

To investigate the gas sensing property, the CeO₂ and Ce_{0.94}Zr_{0.06}O₂ nano-sheets were used as the sensing materials to make a gas sensor, and its response-recovery process to target gas of NH₃ was monitored. The schematic illustration of the gas-sensing testing system is shown in **Fig. 7**. An appropriate bias voltage of 5 V was applied during gas sensing testing. Both the CeO₂ and Ce_{0.94}Zr_{0.06}O₂ nano-sheets based gas sensors showed good ohmic contacts from I-V curves in **Fig. S4**. The response and recovery behaviors of CeO₂ and Ce_{0.94}Zr_{0.06}O₂ nano-sheets based gas sensors were investigated at room temperature. The gas response(R) of sensors is defined as the resistance ratio: $R = R_a/R_g$ [37], (R_g : resistance of sensors in the target gas; R_a : resistance of sensors in air).

The dynamic response-recovery curves and response of gas sensor to NH₃ with various concentrations are shown in **Fig. 8**. From the **Figs. 8a** and **8c**, both the CeO₂ and Ce_{0.94}Zr_{0.06}O₂ nano-sheets based sensors exhibit excellent gas sensing performance to NH₃ even at sub-ppm level. When the NH₃ was injected into the testing chamber, the resistance of sensor was dramatically decreased and reached a steady state immediately. After the NH₃ was extracted from the chamber, the

resistance of the gas sensors was recovered quickly to the initial value, indicating a good reversibility of the sensor. From **Figs. 8b** and **8d**, when the NH₃ concentration is higher than 5 ppm, the relationship between the response and concentrations shows a good linear characteristic.

Compared the sensing performance of two sensors made of the with different nano-sheets materials shown in **Figs. 8b** and **8d**, the gas sensor based on the Ce_{0.94}Zr_{0.06}O₂ nano-sheets shows better response and lower detection limit than those based on the CeO₂ ones. For example, the response of Ce_{0.94}Zr_{0.06}O₂ nano-sheets based sensor is 150 to 500 ppm NH₃, which is 1.2 times higher than that of CeO₂ (with a response of 122). The detection limit of the Ce_{0.94}Zr_{0.06}O₂ nano-sheets based sensor to NH₃ is 100 ppb, which is obviously much lower than the detection limit of CeO₂ of 500 ppb (as shown in **Figs. 8a** and **8b**). Therefore, the addition of Zr ions in the CeO₂ remarkably improves the NH₃ gas sensing performance.

Fig. 9 shows the dynamic response-recovery curves of sensors based on the different Zr doping ratios. The response values towards 500 ppm NH₃ of those sensors are 122, 134, 150 and 29 to pure CeO₂, Ce_{0.98}Zr_{0.02}O₂, Ce_{0.94}Zr_{0.06}O₂ and Ce_{0.90}Zr_{0.10}O₂ respectively. Therefore, the sensor based on Ce_{0.94}Zr_{0.06}O₂ has optimal sensing performance to NH₃.

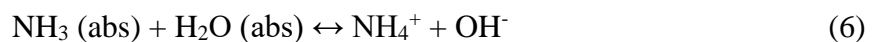
Table 1 Comparison of NH₃ sensing properties of different metal oxide based gas sensors.

Sensing materials	Response to 100 ppm	Detection limit (ppm)	Response at detection limit	Operating temperature (°C)	Refer.
Co ₃ O ₄ nanorods	9.3	0.2	1.2	25	[38]
SnO ₂ nanowire	9	300	9	200	[39]
SiO ₂ @graphene	7.9%	5	2.8	25	[40]

Flower-like Pd-ZnO ₂	81.8	5	7.1	210	[41]
NiO/SnO ₂ nanospheres	55	5	12	300	[42]
PbS/TiO ₂ nanotubes	17.5	2	4	25	[43]
ZnO nanorods	22.6	20	1.02	25	[44]
Hierarchical In ₂ O ₃	~	5	1.9	300	[45]
CeO ₂ nano-sheets	50	0.5	1.1	25	This work
Ce _{0.94} Zr _{0.06} O ₂ nano-sheets	87	0.1	1.2	25	This work

Many NH₃ gas sensors based on metal oxides have been reported in literature, including the metal oxides of Co₃O₄ [46], SnO₂ [39], In₂O₃ [45] and ZnO [47]. **Table 1** selects examples of different types of NH₃ gas sensors in literature. Compared with other types of NH₃ sensors listed in **Table 1**, the Ce_{0.94}Zr_{0.06}O₂ nano-sheets based gas sensor shows the best sensing performance, including a lower detection concentration to 0.1 ppm, higher response and at a much lower working temperature, i.e., room temperature.

The sensing mechanism to NH₃ for the Ce_{0.94}Zr_{0.06}O₂ nano-sheets based sensor could be explained by the electrolytic conductivity of NH₄⁺ and OH⁻. **Fig. 10** shows a schematic diagram of the NH₃ reaction mechanism on the surface of Ce_{0.94}Zr_{0.06}O₂ nano-sheets. Because there are lots of hydroxyl groups on the surface of the Ce_{0.94}Zr_{0.06}O₂ nano-sheets sensing materials, which was verified from XPS analysis, the H₂O molecules can be easily absorbed on the surface of the Ce_{0.94}Zr_{0.06}O₂ nano-sheets at ambient environment and room temperature. Due to the large specific surface area, the amount of absorbed moisture/water molecules would be quite large. When the gas sensor is exposed to NH₃, the NH₃ molecules can be quickly absorbed on the surfaces of the Ce_{0.94}Zr_{0.06}O₂ nano-sheets and then react with H₂O molecules based on the following chemical reaction:

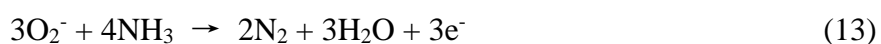


Therefore, the electrolyte of NH_4^+ and OH^- could be produced. Because of the electrolyte conductivity of NH_4^+ and OH^- , the resistance of $\text{Ce}_{0.94}\text{Zr}_{0.06}\text{O}_2$ is decreased accordingly. The chemical reaction (6) is reversible. Thus, when the sensor is exposed to ambient environment (i.e. air), the reversed chemical reaction of Eq. (6) results in formation of NH_3 molecules and NH_3 gas is then desorbed from the surface of $\text{Ce}_{0.94}\text{Zr}_{0.06}\text{O}_2$ nano-sheets. The resistance of sensor is then increased to the initial value. Because desorption of NH_3 is slower than adsorption, the recovery time is longer than the response time (as shown in the **Fig. 8a**).

To verify the sensing mechanism of NH_3 reaction with H_2O molecules on the sensor, we did the NH_3 sensing by increasing the working temperature above 100 °C. At such an elevated temperature, the absorption of H_2O molecules is minimized, and thus the response is almost non-detectable. This clearly indicates that the absorption of water molecules on the surface of the $\text{Ce}_{0.94}\text{Zr}_{0.06}\text{O}_2$ nano-sheets is critical for the good sensing performance at room temperature, but not at high temperature, at which the water molecules would be removed from the surface. Because the $\text{Ce}_{0.94}\text{Zr}_{0.06}\text{O}_2$ nano-sheets have larger specific surface areas and higher pore volumes than those of CeO_2 , which has been proven by the nitrogen adsorption-desorption isotherms measurement shown in **Fig. 5**, the NH_3 gas molecules are more easily diffused and absorbed on the surfaces of $\text{Ce}_{0.94}\text{Zr}_{0.06}\text{O}_2$ nano-sheets, thus resulting a better gas sensing performance than that of the pure CeO_2 .

It have been reported that the doped Zr^{4+} in CeO_2 can introduce much oxygen vacancies on the surface of CeO_2 [48]. At room temperature, the oxygen molecules in

air will be absorbed on the surface of CeO₂ and form surface superoxide complex defects of $Ce^{4+} - O_2^{\bullet-}$ with these oxygen vacancies [49, 50]. The $Ce^{4+} - O_2^{\bullet-}$ was very active [50], which is beneficial to the reaction of $\underline{O_2^-}$ with NH₃ as the following chemical reaction:



The released electrons from the above reaction will lead to the decrease of the resistance sensor, which result in the increased response of the sensor to NH₃. Therefore, the oxygen vacancies resulted from doping of Zr⁴⁺ in CeO₂ also enhanced the response of the NH₃ sensor based on Ce_{0.94}Zr_{0.06}O₂ nano-sheets.

Good selectivity is critical for the NH₃ gas sensor [51]. Therefore, the selectivity of the Ce_{0.94}Zr_{0.06}O₂ nano-sheets based sensor was investigated by comparing the response to C₂H₅OH, CO, H₂, H₂S, NO₂ and ethyl acetate operated at room temperature. The tests were conducted with the same gas concentration of 100 ppm at room temperature. The measurement results are shown in **Fig. 11a**. Clearly, the Ce_{0.94}Zr_{0.06}O₂ nano-sheets based gas sensor exhibited a good response only towards the NH₃ gas. For other detected gases, the response was insignificant. The sensing mechanism of other gases is based on the redox reaction on the surface of metal oxide. However, the surface of Ce_{0.94}Zr_{0.06}O₂ nano-sheets is occupied by many hydroxyl groups, which could delay the redox reactions on the surface, thus the response is not high.

Reproducibility and long-term stability of the Ce_{0.94}Zr_{0.06}O₂ nano-sheets based sensor were further investigated. **Fig. 11b** shows the reproducibility of Ce_{0.94}Zr_{0.06}O₂

nano-sheet based sensor when exposed to 10 ppm and 40 ppm NH₃ gas for four times at room temperature. All the curves of response and recovery processes are reproducible without apparent changes during injection and extraction of ammonia at same NH₃ gas concentration, indicating its good reproducibility. In order to investigate the stability of Ce_{0.94}Zr_{0.06}O₂ nano-sheets based sensor, the response to NH₃ gas were tested by repeatedly exposing the sensor to fixed NH₃ concentration (i.e., 10 ppm and 40 ppm, respectively) within a month at room temperature. The obtained response results are shown in **Fig. 11c**. Clearly, a nearly constant response to 10 ppm and 40 ppm NH₃ gas can be obtained by repeating the tests within the month, indicating that the sensor has a good long-time stability.

4. Conclusions

In this study, we used a facile surfactant-free sol-hydrothermal process to prepared porous Ce_{0.94}Zr_{0.06}O₂ nano-sheets. In the Ce_{0.94}Zr_{0.06}O₂ nano-sheets, Zr⁴⁺ ions were identified to occupy lattice sites of CeO₂ matrix to form a substitutional solid solution. The developed mesoporous structure with pore size around 2.1 nm was formed in the nano-sheets in the Ce_{0.94}Zr_{0.06}O₂ nano-sheets and it have large specific surface area and pore volume. It was proved that the Ce_{0.94}Zr_{0.06}O₂ nano-sheets based NH₃ sensor showed a good response to NH₃, even at 100 ppb level, and good reproducibility, selectivity and long-term stability. The excellent sensing property is not only due to the special mesoporous structures in the nano-sheets, but also due to the plenty of hydroxyl groups on the surface. So, the Ce_{0.94}Zr_{0.06}O₂ nano-sheets based sensor has a good application prospect in NH₃ gas detecting.

Acknowledgments

This work was supported by the Joint Fund of the National Natural Science Foundation of China and the China Academy of Engineering Physics (U1330108). Funding supports from UK Engineering Physics and Science Research Council (EPSRC EP/P018998/1), Newton Mobility Grant (IE161019) through Royal Society and NFSC, and Royal academy of Engineering UK-Research Exchange with China and India are also acknowledged.

References

- [1] K. Mudiyansele, I. Al-Shankiti, A. Foulis, J. Llorca, H. Idriss, Reactions of ethanol over CeO₂ and Ru/CeO₂ catalysts, *Appl. Catal. B-Environ.* 197 (2016) 198-205.
- [2] Y. Huang, B. Long, M. Tang, Z. Rui, M.-S. Balogun, Y. Tong, H. Ji, Bifunctional catalytic material: An ultrastable and high-performance surface defect CeO₂ nanosheets for formaldehyde thermal oxidation and photocatalytic oxidation, *Appl. Catal. B-Environ.* 181 (2016) 779-787.
- [3] J. Zhang, H. Kumagai, K. Yamamura, S. Ohara, S. Takami, A. Morikawa, H. Shinjoh, K. Kaneko, T. Adschiri, A. Suda, Extra-Low-Temperature Oxygen Storage Capacity of CeO₂ Nanocrystals with Cubic Facets, *Nano Lett.* 11 (2011) 361-364.
- [4] L. Fan, C. Wang, M. Chen, B. Zhu, Recent development of ceria-based (nano)composite materials for low temperature ceramic fuel cells and electrolyte-free fuel cells, *J. Power sources.* 234 (2013) 154-174.
- [5] R. Kumar, A. Agrawal, R.K. Nagarale, A. Sharma, High Performance Supercapacitors from Novel Metal-Doped Ceria-Decorated Aminated Graphene, *J. Phys. Chem. C.* 120 (2016) 3107-3116.
- [6] W. Lee, S.-Y. Chen, E. Tseng, A. Gloter, C.-L. Chen, Study of Defect Structure in Ferromagnetic Nanocrystalline CeO₂: Effect of Ionic Radius, *J. Phys. Chem. C.* 120 (2016) 14874-14882.
- [7] Z. Li, X. Niu, Z. Lin, N. Wang, H. Shen, W. Liu, K. Sun, Y.Q. Fu, Z. Wang, Hydrothermally synthesized CeO₂ nanowires for H₂S sensing at room temperature, *J. Alloys compd.* 682 (2016) 647-653.
- [8] N. Izu, S. Nishizaki, T. Itoh, M. Nishibori, W. Shin, I. Matsubara, Gas response, response time and selectivity of a resistive CO sensor based on two connected CeO₂ thick films with various particle sizes, *Sens. Actuators B Chem.* 136 (2009) 364-370.
- [9] Y. Liu, Y. Lei, Pt-CeO₂ nanofibers based high-frequency impedancemetric gas sensor for selective CO and C₃H₈ detection in high-temperature harsh environment, *Sens. Actuators B Chem.* 188 (2013) 1141-1147.
- [10] C.R. Michel, A.H. Martinez-Preciado, CO sensor based on thick films of 3D

-
- hierarchical CeO₂ architectures, *Sens. Actuators B Chem.* 197 (2014) 177-184.
- [11] R.C. Deus, C.R. Foschini, B. Spitova, F. Moura, E. Longo, A.Z. Simões, Effect of soaking time on the photoluminescence properties of cerium oxide nanoparticles, *Ceram. Int.* 40 (2014) 1-9.
- [12] B.H. Min, J.C. Lee, K.Y. Jung, D.S. Kim, B.-K. Choi, W.-J. Kang, An aerosol synthesized CeO₂:Eu³⁺/Na⁺ red nanophosphor with enhanced photoluminescence, *RSC Adv.*, 6 (2016) 81203-81210.
- [13] J.B.R. Carvalho, R.S. Silva, I. Cesarino, S.A.S. Machado, K.I.B. Eguiluz, E.B. Cavalcanti, G.R. Salazar-Banda, Influence of the annealing temperature and metal salt precursor on the structural characteristics and anti-corrosion barrier effect of CeO₂ sol-gel protective coatings of carbon steel, *Ceram. Int.* 40 (2014) 13437-13446.
- [14] Y. Liu, H. Huang, L. Wang, D. Cai, B. Liu, D. Wang, Q. Li, T. Wang, Electrospun CeO₂ nanoparticles/PVP nanofibers based high-frequency surface acoustic wave humidity sensor, *Sens. Actuators B Chem.* 223 (2016) 730-737.
- [15] L. Xu, H. Song, B. Dong, Y. Wang, J. Chen, X. Bai, Preparation and Bifunctional Gas Sensing Properties of Porous In₂O₃-CeO₂ Binary Oxide Nanotubes, *Inorg. Chem.* 49 (2010) 10590-10597.
- [16] W. Wang, Q. Zhu, Q. Dai, X. Wang, Fe doped CeO₂ nanosheets for catalytic oxidation of 1,2-dichloroethane: Effect of preparation method, *Chem. Eng. J.* 307 (2017) 1037-1046.
- [17] G. Zhou, Y. Yao, X. Zhao, X. Liu, B. Sun, A. Zhou, Band gap energies for white nanosheets/yellow nanoislands/purple nanorods of CeO₂, *RSC Adv.* 6 (2016) 59370-59374.
- [18] X.-Q. Fu, P. Feng, C. Wang, T.-H. Wang, Stable electron field emission from CeO₂ nanowires by hydrothermal method, *Chinese Phys. Lett.* 24 (2007) 2423-2425.
- [19] X. Liu, J. Ding, X. Lin, R. Gao, Z. Li, W.-L. Dai, Zr-doped CeO₂ nanorods as versatile catalyst in the epoxidation of styrene with tert-butyl hydroperoxide as the oxidant, *Appl. Catal. A-Gen.* 503 (2015) 117-123.
- [20] J. Wei, Z. Yang, H. Yang, T. Sun, Y. Yang, A mild solution strategy for the synthesis of mesoporous CeO₂ nanoflowers derived from Ce(HCOO)₃,

CrystEngComm. 13 (2011) 4950.

[21] Q. Dai, S. Bai, H. Li, W. Liu, X. Wang, G. Lu, Template-free and non-hydrothermal synthesis of CeO₂ nanosheets via a facile aqueous-phase precipitation route with catalytic oxidation properties, CrystEngComm. 16 (2014) 9817-9827.

[22] H.I. Chen, H.Y. Chang, Synthesis and characterization of nanocrystalline cerium oxide powders by two-stage non-isothermal precipitation, Solid State Commun. 133 (2005) 593-598.

[23] L. Liao, H.X. Mai, Q. Yuan, H.B. Lu, J.C. Li, C. Liu, C.H. Yan, Z.X. Shen, T. Yu, Single CeO₂ Nanowire Gas Sensor Supported with Pt Nanocrystals: Gas Sensitivity, Surface Bond States, and Chemical Mechanism, J. Phys. Chem. C. 112 (2008) 9061-9065.

[24] D. Barreca, A. Gasparotto, C. Maccato, C. Maragno, E. Tondello, E. Comini, G. Sberveglieri, Columnar CeO₂ nanostructures for sensor application, Nanotechnology. 18 (2007) 125502.

[25] C.R. Michel, A.H. Martínez-Preciado, CO sensor based on thick films of 3D hierarchical CeO₂ architectures, Sens. Actuators B Chem. 197 (2014) 177-184.

[26] Y. Yang, C. Tian, L. Sun, R. Lü, W. Zhou, K. Shi, K. Kan, J. Wang, H. Fu, Growth of small sized CeO₂ particles in the interlayers of expanded graphite for high-performance room temperature NO_x gas sensors, J. Mater. Chem. A. 1 (2013) 12742.

[27] Y.-J. Chen, G. Xiao, T.-S. Wang, F. Zhang, Y. Ma, P. Gao, C.-L. Zhu, E. Zhang, Z. Xu, Q.-h. Li, Synthesis and enhanced gas sensing properties of crystalline CeO₂/TiO₂ core/shell nanorods, Sens. Actuators B Chem. 156 (2011) 867-874.

[28] H. Ibrahim, Y. Temerk, A novel electrochemical sensor based on B doped CeO₂ nanocubes modified glassy carbon microspheres paste electrode for individual and simultaneous determination of xanthine and hypoxanthine, Sens. Actuators B Chem. 232 (2016) 125-137.

[29] A.V. Rajgure, N.L. Tarwal, J.Y. Patil, L.P. Chikhale, R.C. Pawar, C.S. Lee, I.S. Mulla, S.S. Suryavanshi, Gas sensing performance of hydrothermally grown

-
- CeO₂-ZnO composites, *Ceram. Int.* 40 (2014) 5837-5842.
- [30] M. Sanchez-Dominguez, L.F. Liotta, G. Di Carlo, G. Pantaleo, A.M. Venezia, C. Solans, M. Boutonnet, Synthesis of CeO₂, ZrO₂, Ce_{0.5}Zr_{0.5}O₂, and TiO₂ nanoparticles by a novel oil-in-water microemulsion reaction method and their use as catalyst support for CO oxidation, *Catal. Today*. 158 (2010) 35-43.
- [31] X. Liu, W. Liu, X. Zhang, L. Han, C. Zhang, Y. Yang, Zr-doped CeO₂ Hollow slightly-truncated nano-octahedrons: One-pot synthesis, characterization and their application in catalysis of CO oxidation, *Cryst. Res. Technol.* 49 (2014) 383-392.
- [32] C. Feng, J. Zhang, Y. He, C. Zhong, W. Hu, L. Liu, Y. Deng, Sub-3 nm Co₃O₄ Nanofilms with Enhanced Supercapacitor Properties, *ACS nano*. 9 (2015) 1730-1739.
- [33] D. Zhang, H. Fu, L. Shi, C. Pan, Q. Li, Y. Chu, W. Yu, Synthesis of CeO₂ nanorods via ultrasonication assisted by polyethylene glycol, *Inorg. Chem.* 46 (2007) 2446-2451.
- [34] A.Q. Wang, P. Panchaipecth, R.M. Wallace, T.D. Golden, X-ray photoelectron spectroscopy study of electrodeposited nanostructured CeO₂ films, *J. Vac. Sci. Technol. B*. 21 (2003) 1169.
- [35] Y. Wang, J. Liu, X. Cui, Y. Gao, J. Ma, Y. Sun, P. Sun, F. Liu, X. Liang, T. Zhang, G. Lu, NH₃ gas sensing performance enhanced by Pt-loaded on mesoporous WO₃, *Sens. Actuators B Chem.* 238 (2017) 473-481.
- [36] Y. Huang, W. Chen, S. Zhang, Z. Kuang, D. Ao, N.R. Alkurd, W. Zhou, W. Liu, W. Shen, Z. Li, A high performance hydrogen sulfide gas sensor based on porous α -Fe₂O₃ operates at room-temperature, *Appl. Surf. Sci.* 351 (2015) 1025-1033.
- [37] Z. Li, Z. Lin, N. Wang, Y. Huang, J. Wang, W. Liu, Y. Fu, Z. Wang, Facile synthesis of α -Fe₂O₃ micro-ellipsoids by surfactant-free hydrothermal method for sub-ppm level H₂S detection, *Mater. Design*. 110 (2016) 532-539.
- [38] Z. Li, Z. Lin, N. Wang, J. Wang, W. Liu, K. Sun, Y.Q. Fu, Z. Wang, High precision NH₃ sensing using network nano-sheet Co₃O₄ arrays based sensor at room temperature, *Sens. Actuators B Chem.* 235 (2016) 222-231.
- [39] L.V. Thong, N.D. Hoa, D.T.T. Le, D.T. Viet, P.D. Tam, A.-T. Le, N.V. Hieu, On-chip fabrication of SnO₂-nanowire gas sensor: The effect of growth time on sensor

-
- performance, *Sens. Actuators B Chem.* 146 (2010) 361-367.
- [40] D. Huang, Z. Yang, X. Li, L. Zhang, J. Hu, Y. Su, N. Hu, G. Yin, D. He, Y. Zhang, Three-dimensional conductive networks based on stacked SiO₂@graphene frameworks for enhanced gas sensing, *Nanoscale*. 9 (2017) 109-118.
- [41] Y. Zeng, Z. Lou, L. Wang, B. Zou, T. Zhang, W. Zheng, G. Zou, Enhanced ammonia sensing performances of Pd-sensitized flowerlike ZnO nanostructure, *Sens. Actuators B Chem.* 156 (2011) 395-400.
- [42] L. Wang, J. Deng, T. Fei, T. Zhang, Template-free synthesized hollow NiO–SnO₂ nanospheres with high gas-sensing performance, *Sens. Actuators B Chem.* 164 (2012) 90-95.
- [43] Y. Liu, L. Wang, H. Wang, M. Xiong, T. Yang, G.S. Zakharova, Highly sensitive and selective ammonia gas sensors based on PbS quantum dots/TiO₂ nanotube arrays at room temperature, *Sens. Actuators B Chem.* 236 (2016) 529-536.
- [44] S. Anantachaisilp, S.M. Smith, C. Ton-That, T. Osotchan, A.R. Moon, M.R. Phillips, Tailoring Deep Level Surface Defects in ZnO Nanorods for High Sensitivity Ammonia Gas Sensing, *J. Phys. Chem. C*. 118 (2014) 27150-27156.
- [45] H. Jiang, L. Zhao, L. Gai, L. Ma, Y. Ma, M. Li, Hierarchical rh-In₂O₃ crystals derived from InOOH counterparts and their sensitivity to ammonia gas, *CrystEngComm*. 15 (2013) 7003.
- [46] J. Deng, R. Zhang, L. Wang, Z. Lou, T. Zhang, Enhanced sensing performance of the Co₃O₄ hierarchical nanorods to NH₃ gas, *Sens. Actuators B Chem.* 209 (2015) 449-455.
- [47] L. Wang, Z. Lou, T. Fei, T. Zhang, Templating synthesis of ZnO hollow nanospheres loaded with Au nanoparticles and their enhanced gas sensing properties, *J. Mater. Chem.* 22 (2012) 4767.
- [48] C.T. Campbell, C.H.F. Peden, Chemistry - Oxygen vacancies and catalysis on ceria surfaces, *Science*. 309 (2005) 713-714.
- [49] Y. Li, B. Zu, Y. Guo, K. Li, H. Zeng, X. Dou, Surface Superoxide Complex Defects-Boosted Ultrasensitive ppb-Level NO₂ Gas Sensors, *Small*. 12 (2016) 1420-1424.

-
- [50] S. Wang, D. Huang, S. Xu, W. Jiang, T. Wang, J. Hu, N. Hu, Y. Su, Y. Zhang, Z. Yang, Two-dimensional NiO nanosheets with enhanced room temperature NO₂ sensing performance via Al doping, *Phys.Chem.Chem.Phys.* 19 (2017) 19043-19049.
- [51] T. Wang, D. Huang, Z. Yang, S. Xu, G. He, X. Li, N. Hu, G. Yin, D. He, L. Zhang, A Review on Graphene-Based Gas/Vapor Sensors with Unique Properties and Potential Applications, *Nano-Micro Lett.* 8 (2016) 95-119.

Fig. 1. XRD spectra of CeO₂ and Ce_{0.94}Zr_{0.06}O₂ samples.

Fig. 2. (a) SEM, (b) TEM and (c) HRTEM images of CeO₂; (d) SEM, (e) TEM and (f) HRTEM images of Ce_{0.94}Zr_{0.06}O₂. (Inset images in Figs. 2c and 2f were selected area electron diffraction (SAED) pattern).

Fig. 3. 3D AFM image of Ce_{0.94}Zr_{0.06}O₂ nano-sheets.

Fig. 4. TEM image (a) and the corresponding elemental mapping analysis of Ce mapping image (b) and Zr mapping image (c).

Fig. 5. N₂ adsorption isotherms of CeO₂ and Ce_{0.94}Zr_{0.06}O₂ nano-sheets. (inset: pore size distributions).

Fig. 6. (a) Ce 3d and (b) O 1s XPS spectra of CeO₂ and Ce_{0.94}Zr_{0.06}O₂ nano-sheets; (c) Zr 3d XPS spectra of Ce_{0.94}Zr_{0.06}O₂ nano-sheets.

Fig. 7. The schematic illustration of the gas-sensing testing system.

Fig. 8. Fig. 8. Dynamic response-recovery curve and response data of gas sensors to NH₃ gas with various concentrations at room temperature. ((a, b) CeO₂ based gas sensor (c,d) Ce_{0.94}Zr_{0.06}O₂ nano-sheets based gas sensor).

Fig. 9. The dynamic response-recovery curves of sensor based on the different Zr doping ratios to 500 ppm NH₃ gas at room temperature.

Fig. 10. Schematic diagram of the NH₃ reaction mechanism on the surface of Ce_{0.94}Zr_{0.06}O₂ nano-sheets.

Fig. 11. (a) Selectivity, (b) Reproducibility and (c) Long-term stability of the Ce_{0.94}Zr_{0.06}O₂ nano-sheets based sensor at the room temperature.